Optical Materials: X 14 (2022) 100155

Contents lists available at ScienceDirect

Optical Materials: X

journal homepage: www.journals.elsevier.com/optical-materials-x

High-resolution spectroscopic studies of random strains in ferroelastic domains in a $LaAlO_3:Tm^{3+}$ single crystal

K.N. Boldyrev [a,*], N.M. Abishev [b], I.E. Mumdzi [b], S.I. Nikitin [b], B.Z. Malkin [b], R.V. Yusupov [b], M.N. Popova [a]

[a] Institute of Spectroscopy RAS, Troitsk, Moscow, 108840, Russia
[b] Kazan Federal University, Institute of Physics, Kazan, 420008, Russia

ARTICLE INFO

Keywords:
Optical spectra
Crystal-field levels
Ferroelastic domains
Deformational fine structure
Random strains
Distribution function

ABSTRACT

Comprehensive spectroscopic, magnetization, and theoretical studies of a $LaAlO_3:Tm^{3+}$ single crystal in the ferroelastic $R\bar{3}c$ phase are reported. The Tm^{3+} ions substitute for the La^{3+} ions at sites with the D_3 symmetry. High-resolution absorption, photoluminescence, and site-selective emission and excitation spectra were measured in the broad spectral range from 4000 to 28000 cm^{-1} at temperatures 4.2–5 K. The two-fold degeneracy of the ground state of Tm^{3+} was uncovered by magnetization measurements. Energies and symmetry properties of wave functions of crystal-field levels of the Tm^{3+} ions were determined and successfully reproduced by crystal-field calculations. Specific profiles with a dip at the center of spectral lines corresponding to transitions involving non-Kramers doublets give evidence for random strains in the studied multidomain sample. The value of 0.1–0.8 cm^{-1} of deformational splitting of non-Kramers doublets exceeds hyperfine splittings by more than an order of magnitude. The observed line shapes were successfully modeled assuming the interaction of Tm^{3+} ions with random deformations described by the generalized two-dimensional Lorentzian distribution with the width of $(7 \pm 0.5)\cdot 10^{-4}$. The simulation was performed using the electron-deformation coupling constants calculated in the framework of the exchange-charge model.

1. Introduction

Crystalline lanthanum aluminate $LaAlO_3$ (LAO), a pseudo-cubic perovskite, is a multifunctional material that finds applications in many different technologies. It is used as a substrate for ferroelectrics, high-Tc superconductors, and other functional materials [1,2], as a catalyst [3], and as gate dielectrics in transistors [4,5]. LAO crystals doped with rare-earth (RE) ions are used as efficient luminophors [6–13] and laser hosts [14]. A broad intrinsic energy gap of LAO (~5.5 eV [15]) is favorable for UV photonic applications.

The lanthanum aluminate crystallizes in a cubic perovskite structure with the space group $Pm\bar{3}m$ and at the temperature $T_S = 813$ K undergoes an improper ferroelastic phase transition to a rhombohedral phase (space group $R\bar{3}c$) driven by rotation of the AlO_6 octahedra about one of the cubic threefold symmetry axes [16,17]. At room temperature and below, one deals with the rhombohedral $R\bar{3}c$ structure. Its unit cell contains six formula units; La^{3+} ions are at the 6*a* sites (having the D_3 point symmetry group) with the coordinates (0,0,*c*/4), Al^{3+} ions reside at the 6*b* sites (0,0,0), and O^{2-} ions occupy the 18*e* sites (*ax*,0,*c*/4); here $a = 5.36$ Å, $c = 13.086$ Å are the lattice constants of $LaAlO_3$ and $x = 0.5281$ is the structure parameter of the oxygen sublattices [16]. There are 12 O^{2-} ions in the nearest surrounding of a La^{3+} ion at distances from 2.516 Å to 2.814 Å.

As there are four equivalent C_3 axes in the parent cubic phase, four distinct ferroelastic twin domain variants occur in LAO crystals upon cooling below T_S [17–19]. Domain boundaries serve as a source of internal strains in microscopically inhomogeneous samples; they can strongly affect the spectral properties of activator centers in LAO.

The reported spectra of LAO doped with different RE ions demonstrate an appreciable inhomogeneous broadening [6–14,20,21]. Recently, in the spectra of LAO single crystals doped with non-Kramers Ho^{3+} ions, we have detected specific line shapes with a narrow dip at the center of the lines corresponding to singlet-doublet transitions of Ho^{3+} [22]. Such line shapes were observed also in other RE-doped crystals,

Abbreviations: RE, rare-earth; CF, crystal field; LAO, $LaAlO_3$; PL, photoluminescence; IR, irreducible representations; ED, electric-dipole; MD, magnetic-dipole.

* Corresponding author.
E-mail address: kn.boldyrev@gmail.com (K.N. Boldyrev).

https://doi.org/10.1016/j.omx.2022.100155
Received 30 April 2022; Accepted 2 May 2022
Available online 13 May 2022

they were shown to result from random strains induced by defects in the crystal lattice [23–26]. Using the theory developed previously [24,26], which took into account an interaction of impurity ions with the field of random deformations induced by point defects in an elastically anisotropic crystal lattice, we were able to successfully reproduce the main specific features of line shapes in the spectra of LAO:Ho [22]. However, the concentration of point defects required for quantitative agreement between the calculated and measured line profiles was more than five times higher than the nominal concentration of Ho^{3+} ions (0.5 wt%), and the nature of possible intrinsic lattice defects remained unknown. In Ref. [22], attention was also paid to a specific ferroelastic mesoscopic twin-domain structure in $LaAlO_3$ single crystals, but the simulated spectral line profiles based on the introduced phenomenological one-dimensional distribution function of random shear deformations contradicted to the observed line shapes with much wider wings.

Here we introduce a two-dimensional distribution function of random deformations generated by twin-domain boundaries in $LaAlO_3$ single crystals in the ferroelastic phase and use it for elucidating the nature of an anomalously strong broadening of spectral lines and of a fine structure of transitions involving orbitally degenerate energy levels of impurity non-Kramers ions, observed in the high-resolution spectra of LaAO:Tm^{3+}.

Previously, absorption and emission spectra of LAO:Tm^{3+} were measured with a medium resolution at temperatures of 10–300 K in Ref. [21]. In the present work, high-resolution optical absorption and luminescence spectra of LAO single crystal doped with the Tm^{3+} ions were measured in a wide range of wavelengths. For more accurate identification of spectral lines and determination of crystal-field (CF) energies, the methods of site-selective laser spectroscopy were also used. The analysis of the registered spectra allowed us to determine CF parameters and successfully reproduce the measured CF energies. The wave functions obtained from CF calculations were used to calculate the hyperfine structure in the spectra of Tm^{3+} in LAO and to model deformation splittings of the spectral lines.

The paper is organized as follows. After an Introduction, in Sec. 2, we describe the samples and the details of optical measurements. Section 3 reports on the temperature-dependent optical absorption and luminescence spectra and the results of selective-excitation measurements. Section 4 is devoted to the crystal-field calculations. In Section 5, modeling of deformational fine structures of spectral lines based on the two-dimensional distribution function of shear deformations is performed. The paper ends with a Conclusion.

2. Experimental details

A single crystal of $LaAlO_3$ doped with Tm^{3+} (0.5 wt%) was grown by the Czochralski method at Union Carbide Corporation. The sample in the shape of a parallelepiped with dimensions of $4 \times 3 \times 3$ mm was cut from the bulk and polished. Fig. 1 shows microphotographs of our LAO-Tm sample in the transmitted light with clearly visible domains. Numerous scratches are also visible, and the picture of domains is rather complicated.

Photoluminescence (PL) of the crystal was excited with either a pulsed tunable dye laser (Littrow type oscillator and amplifier, linewidth of about 1 Å) pumped by the second or third harmonic of a Q-switched Nd-YAG laser (LQ129, Solar LS) or a Ti:sapphire tunable laser with linewidth of about 0.4 Å (LX325, Solar LS) pumped by the second harmonic of a Q-switched Nd-YAG laser (LQ829, Solar LS). The laser wavelength was calibrated by a high-resolution wide-range wavelength meter (SHR, Solar LS) with an accuracy better than 0.1 Å. The spectra were analyzed with an MDR-23 monochromator (spectral resolution was about 1 Å). The fluorescence signal was detected by a cooled photomultiplier (PMT-106 or PMT-83) in the photon-counting mode. The studied crystals were kept in helium vapor at a temperature of 4.2 K.

High-resolution polarized transmission and luminescence spectra in a wide spectral range (4000 - 28000 cm^{-1}) were measured with a high-resolution Fourier spectrometer Bruker IFS 125 HR equipped with Si and InSb detectors. The spectral resolution for the absorption measurements was up to 0.01 cm^{-1}. The photoluminescence was excited by a cw multimode diode laser (the wavelength 472 nm). The laser radiation was focused on the sample in a spot of about 0.5 mm in diameter. Low-temperature (5–10 K) measurements were performed using a closed-cycle helium cryostat Cryomech PT403.

The magnetization of the sample was measured using a PPMS-9 magnetometer.

3. Experimental results

Low-temperature unpolarized transmission and photoluminescence spectra of LAO:Tm^{3+} in the whole studied spectral range are shown in Fig. 2. A number of low-intensity lines observed between optical multiplets of Tm^{3+} ions and ascribed to other impurity rare-earth ions with

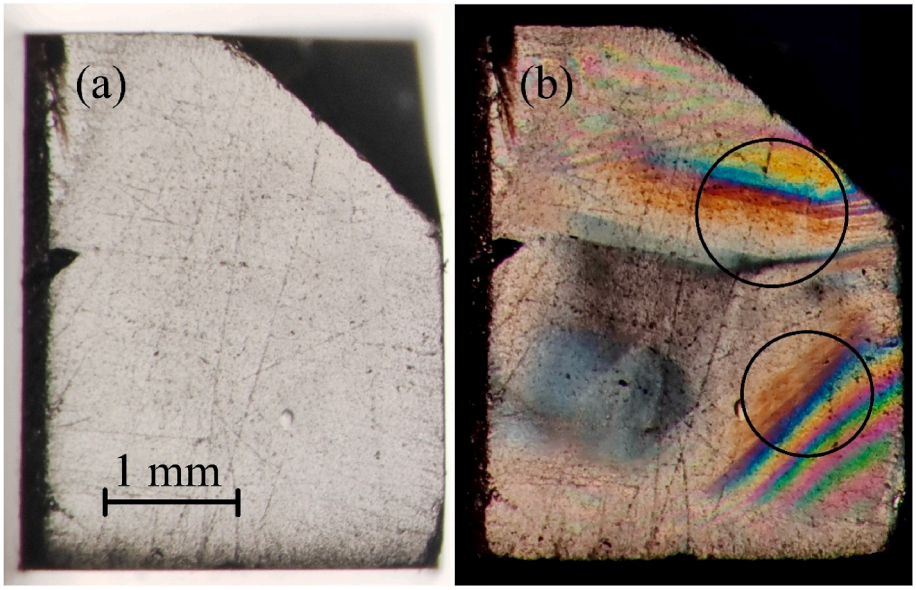

Fig. 1. Microphotographs of the LAO: Tm (0.5 at. %) sample (a) in the unpolarized light and (b) between crossed polarizers. Regions with the most clear domain structures are marked by circles.

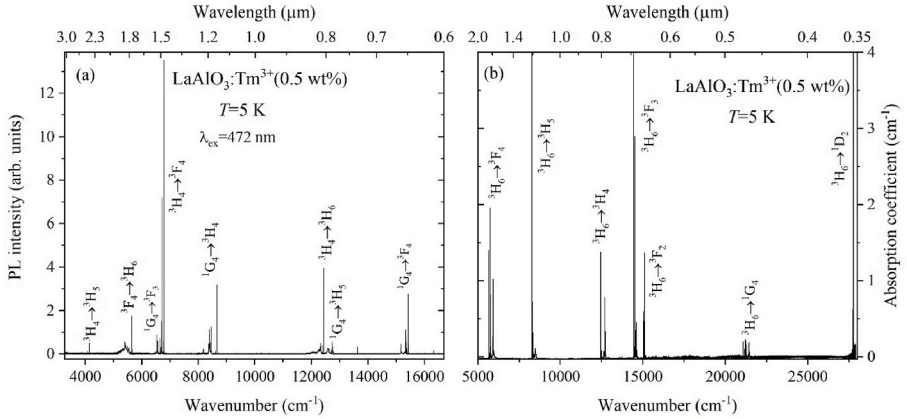

Fig. 2. Unpolarized (a) luminescence and (b) absorption spectra of a LAO:Tm (0.5 wt%) single crystal at 5 K. In (a), the excitatation wavelength was 472 nm.

concentrations less than 0.01 wt% are not shown in Fig. 2b. Numerous narrow lines in the absorption and excitation spectra correspond to the optical transitions from the ground state to excited multiplets, indicated in Fig. 3. Lines in the luminescence spectra are due to transitions from the lowest CF sublevels of the excited multiplets $^1G_4$, $^3H_4$, and $^3F_4$ to the lower-lying CF levels (see Fig. 3).

Identification of spectral lines corresponding to zero-phonon transitions in the main optical centers formed by the impurity Tm^{3+} ions at La^{3+} sites with the D_3 point symmetry was performed based on selectively excited metastable CF sublevels. In the D_3 symmetry position, wave functions of non-Kramers ions (like Pr^{3+}, Tm^{3+}, and Ho^{3+}) transform according to Γ_1 and Γ_2 one-dimensional and Γ_3 two-dimensional irreducible representations (IR).

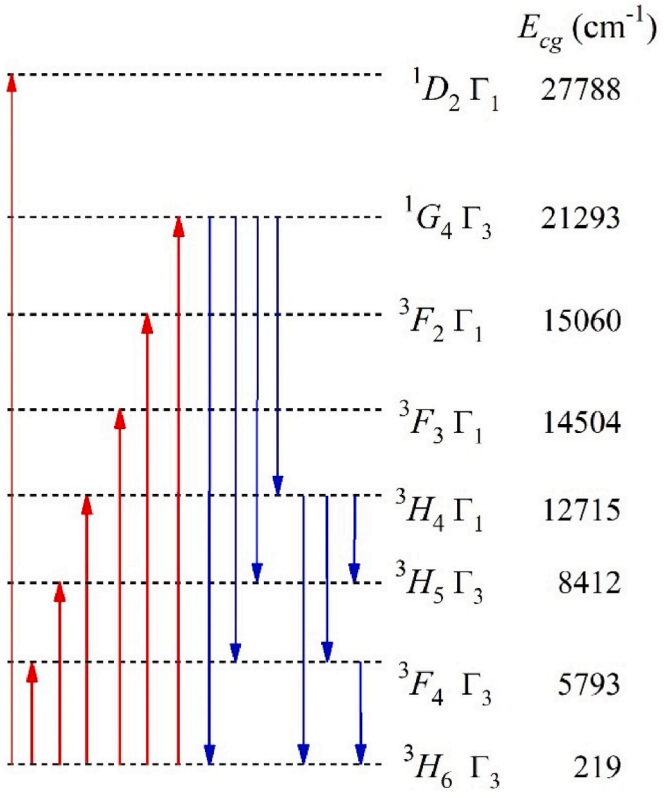

Fig. 3. Scheme of energy levels for Tm^{3+} in LAO. Symmetry of the lower sublevels and energies of centers of gravity (E_{cg}) of multiplets are presented. Red (blue) arrows indicate optical transitions in the registered absorption (emission) spectra. (For interpretation of the references to colour in this figure legend, the reader is referred to the Web version of this article.)

Due to the symmetry selection rules (see, e.g., Table I in Ref. [22]), $\Gamma_1 \rightarrow \Gamma_1$ and $\Gamma_2 \rightarrow \Gamma_2$ optical transitions are strictly forbidden; $\Gamma_1 \leftrightarrow \Gamma_2$ transitions are allowed in the electric-dipole (ED) approximation for the light polarized along the local z axis ($\boldsymbol{E} \,||\, z$), which coincides with the C_3 symmetry axis in domains, and in the magnetic-dipole (MD) approximation for the light polarized perpendicular to the z axis ($\boldsymbol{E} \perp z$); Γ_1 (Γ_2) $\leftrightarrow \Gamma_3$ transitions should manifest themselves as ED for $\boldsymbol{E} \perp z$ and as MD for $\boldsymbol{E} \,||\, z$; $\Gamma_3 \rightarrow \Gamma_3$ transitions are allowed in any polarization both as ED and MD ones. However, because of the microscopic crystal lattice inhomogeneity caused by the irregular domain structure of the studied sample, we found it impossible to perform the detailed analysis of the spectra in the polarized radiation.

Thulium is a monoisotopic element (^{169}Tm) with a non-zero nuclear spin moment $I = 1/2$. Magnetic hyperfine interactions and random crystal lattice strains split CF non-Kramers Γ_3 doublets. A fine structure of spectral lines corresponding to transitions which involve non-Kramers doublets can be observed in the high-resolution optical spectra and gives an additional possibility to check the CF level identification. Fig. 4 presents examples of the observed splittings of the lines corresponding to singlet – doublet (*a,c,e*) and doublet – doublet (*b,d,f*) transitions between CF levels in the absorption and PL spectra of LAO:Tm^{3+} (assignments of lines to concrete transitions is explained below in this Section). A peculiar triplet structure is observed in the line profile of the doublet – doublet transition in Fig. 4*b*. Besides the lines presented in Fig. 4*a, c-f*, a doublet structures with the widths 0.65, 0.15 and 0.24 cm^{-1} of dips at the line center were observed in line profiles at 8648.7 cm^{-1} [$^1G_4(A\Gamma_3) \Rightarrow {}^3H_4(A\Gamma_1)$], 12433.6 cm^{-1} [$^3H_6(A\Gamma_3) \Rightarrow {}^3H_4(A\Gamma_1)$] and 4144.7 cm^{-1} [$^3H_4(A\Gamma_1) \Rightarrow {}^3H_5(A\Gamma_3)$], respectively, corresponding to transitions indicated in square brackets.

First of all, to identify lines in the registered spectra, we determined the ground state-symmetry for the impurity Tm^{3+} ions. As follows from the PL measurements, the gap between two lower CF sublevels of the ground multiplet $^3H_6$ equals 60 K, and, at the temperature 2 K, only the lowest sublelevel is populated. The measured field dependence of the sample magnetization at this temperature (see Fig. 5) demonstrates a saturation and evidences unambiguously the Γ_3 doublet ground state with the *g*-factor close to 10. This conclusion is confirmed by the preliminary calculation of the CF energies where we used CF parameters determined earlier for the impurity Er^{3+} ions in $LaAlO_3$ [27].

The observed triplet structure of the absorption transition from the doublet ground state $^3H_6(A\Gamma_3)$ to the lowest CF sublevel of the $^3H_5$ multiplet indicates the Γ_3 symmetry of this sublevel (see Fig. 4*b*). A comparison of doublet structures of the spectral lines in Fig. 4*e* and *f* which involve the lowest sublevel of the $^3F_4$ multipet allows us to ascribe these lines with narrow and wide dips at the center to singlet-doublet $^3H_4(A\Gamma_1$ or $A\Gamma_2) \Rightarrow {}^3F_4(A\Gamma_3)$ and doublet-doublet $^3H_6(A\Gamma_3) \Rightarrow {}^3F_4(A\Gamma_3)$

Table 1
Energies (cm^{-1}), symmetries, *g*-factors, and hyperfine splittings Δ_{hf} (cm^{-1}) of the CF levels for impurity Tm^{3+} ions in $LaAlO_3$.

Multiplet $^{2S+1}L_J$	CF energy			Symmetry	g-factor	$10^3\Delta_{hf}$
	Exper. [21]	Exper.	Theory	Theory		
1	2	3	4	5 6		7
$^3H_6$	0	0	0	A Γ_3	9.595	52
	42	42	41.2	B Γ_1	0	0
	(94) 111	110	107.5	C Γ_3	4.037	23
	169	165	173.3	D Γ_2	0	0
	(216) 247	243	243.6	E Γ_1	0	0
	322	327	316.7	F Γ_3	2.336	14
	–	–	354.5	G Γ_1	0	0
	–	–	368.1	H Γ_3	1.343	8
	–	443	447.1	I Γ_2	0	0
$^3F_4$	5653	5652	5652.1	A Γ_3	0.064	1
	(5696) 5730	5729.2	5734.7	B Γ_2	0	0
	5746	5744.5	5746.8	C Γ_3	0.937	6
	(5773, 5884)	–	5872.8	D Γ_1	0	0
	5905	5905	5898.4	E Γ_3	5.824	33
	5915	5914	5932.1	F Γ_1	0	0
$^3H_5$	8290, 8337	8289.2 8337.2	8289.5 8345.7	A Γ_3 B Γ_2	6.005 0	47 0
	8357 (8378) (8406) 8472	8366	8346.4	C Γ_3	7.615	59
	–	8459	8467.1	D Γ_3	0.671	6
	–	8460	8468.4	E Γ_1	0	0
	–	8505	8502.3	F Γ_3	1.651	15
		–	8502.7	G Γ_2	0	0
$^3H_4$	12437	12434	12431	A Γ_1	0	0
	12642	12639	12638	B Γ_3	5.545	52
	12678	12677	12708	C Γ_2	0	0
	12697	12695	12713	D Γ_1	0	0
	12722	12720	12727	E Γ_3	0.101	3
	12907	12903	12925	F Γ_3	0.429	3
	14443	14440	14437	A Γ_3	1.251	7
	14484	14480	14481	B Γ_1	0	0
$^3F_3$	14506	14503	14521	C Γ_2	0	0
	14535	14535	14530	D Γ_3	3.231	22
	(14548) 14599	14599	14589	E Γ_2	0	0
$^3F_2$	–	–	15002	A Γ_1	0	0
	15043	15039	15047	B Γ_3	0.994	11
	15115 (15180)	15113	15100	C Γ_3	2.330	28
$^1G_4$	(20759) 21081	21086	21083	A Γ_3	0.985	9
		21219	21226	B Γ_2	0	0
		21264	21256	C Γ_3	0.517	6
	–	21431	21414	D Γ_1	0	0
	–	21440	21424	E Γ_3	3.984	40
	–	–	21474	F Γ_1	0	0
$^1D_2$	27739	27739	27748	A Γ_1	0	0
	27774	27774	27764	B Γ_3	2.244	12
	27867	–	27834	C Γ_3	4.469	27

transitions, respectively. From the doublet structures of the PL transition that involves the singlet lowest sublevel of the $^3H_4$ multiplet, we find the Γ_3 symmetry for the lowest CF sublevel of the $^1G_4$ multiplet. This information, supplemented by the preliminary CF calculations, allowed us to construct a self-consistent scheme of CF energy levels for impurity Tm^{3+} ions at La^{3+} sites in $LaAlO_3$.

Additional (mostly weak) spectral lines are observed almost in all optical multiplets, as in Ref. [21]. Corresponding additional CF energy levels are shown in parentheses in Table 1, column 2. We suppose that these lines distinguished by a comparison of absorption, photoluminescence and site-selective excitation spectra (see Figs. 6–9) can be ascribed to strongly perturbed optical centers of impurity ions at sites close to domain boundaries.

Column 3 in Table I contains experimentally determined energies and symmetries of the CF levels for Tm^{3+} in LAO (experimental data from Ref. [21] are in column 2). In particular, the CF structure of the ground multiplet $^3H_6$ was determined from the PL spectra corresponding to transitions from the lowest CF sublevels of the $^3F_4$ and $^3H_4$ multiplets having different symmetry properties, namely, from the AΓ_3 doublet and AΓ_1 singlet, respectively (see Fig. 6).

The CF structure of the $^1G_4$ multiplet was determines from the absorption and site-selective excitation spectra (emission was registered at the frequency 20843.28 cm^{-1} of the transition $^1G_4$(AΓ_3))⇒$^3H_6$(EΓ_1), see Fig. 7, lines 1 and 2, respectively). Capital letters correspond to the energy levels presented in Table 1. Here, three transitions marked by stars remain unidentified.

Fig. 8 illustrates the decoding of the CF structure of the $^3F_3$ multiplet. A comparison of the transition frequencies in the absorption $^3H_6$(AΓ_3)⇒$^3F_3$ (red line 1) and PL $^1G_4$(AΓ_3) ⇒$^3F_3$ (violet line 2) spectra and in the selective laser excitation of the emission (blue line 3) registered at the frequency 12324.4 cm^{-1} of the transition $^3H_4$(AΓ_1)⇒$^3H_6$(CΓ_3) allowed us to distinguish three weak spectral lines corresponding to unidentified optical centers.

One more example of CF structure registered by different spectroscopic methods is shown in Fig. 9 for the $^3F_4$ multiplet. Here, we compare two PL spectra, $^1G_4$(AΓ_3) ⇒$^3F_4$ (red line 1) and $^3H_4$(AΓ_1) ⇒$^3F_4$ (black line 2) and the emission $^1G_4$(AΓ_3) ⇒$^3F_4$ (violet line 3) selectively excited at the frequency 21431.5 cm^{-1} of the transition $^3H_6$(AΓ_3)⇒$^1G_4$(DΓ_1) with the absorption spectrum $^3H_6$(AΓ_3) ⇒$^3F_4$ (blue line 4).

4. Crystal-field calculations: CF levels and hyperfine structure

The energies of the CF levels of the ground and excited multiplets of the Tm^{3+} ions determined from the measured optical spectra were analyzed using the Hamiltonian operating in the space of 91 states of the ground electronic $4f^{10}$ configurations. The considered single-ion Hamiltonian

$$H_0 = H_{FI} + H_{CF} \tag{1}$$

contains the energy of a free ion (H_{FI}) and the energy of 4*f* electrons in the crystal field (H_{CF}).

The free-ion Hamiltonian is written in the standard form [28],

$$H_{FI} = \zeta\sum_k \mathbf{l}_k\mathbf{s}_k + \alpha\hat{\mathbf{L}}^2 + \beta\hat{G}(G_2) + \gamma\hat{G}(R_7) + \sum_q\left(F^q\hat{f}_q + P^q\hat{p}_q + M^q\hat{m}_q\right), \tag{2}$$

where $\boldsymbol{l}_k$ and $\boldsymbol{s}_k$ are the operators of the orbital and spin moments of 4*f* electrons, respectively; $\mathbf{L} = \sum_k \mathbf{l}_k$ is the operator of the total orbital moment; F^q are the Slater parameters of the electrostatic interactions between 4*f* electrons; ζ is the spin-orbit coupling constant; α, β, γ are the parameters of two-particle electrostatic interconfigurational interactions; the parameters P^q and M^q define the spin-orbit and spin-spin interactions between 4*f* electrons, respectively.

The Hamiltonian of the Tm^{3+} ion at the La^{3+} site in the crystal field of the D_3 symmetry, in the Cartesian system of coordinates with the *z* axis along the C_3 symmetry axis and the *x* axis along the local C_2 symmetry axis in the crystallographic *ab* plane is defined by six real CF parameters B_p^k and has the following form

$$H_{CF} = B_2^0C_0^{(2)} + B_4^0C_0^{(4)} + B_4^3\left(C_{-3}^{(4)} - C_3^{(4)}\right) + \ldots$$
$$B_6^0C_0^{(6)} + B_6^3\left(C_{-3}^{(6)} - C_3^{(6)}\right) + B_6^6\left(C_6^{(6)} + C_{-6}^{(6)}\right) \tag{3}$$

where $C_k^{(p)}$ are spherical tensor operators.

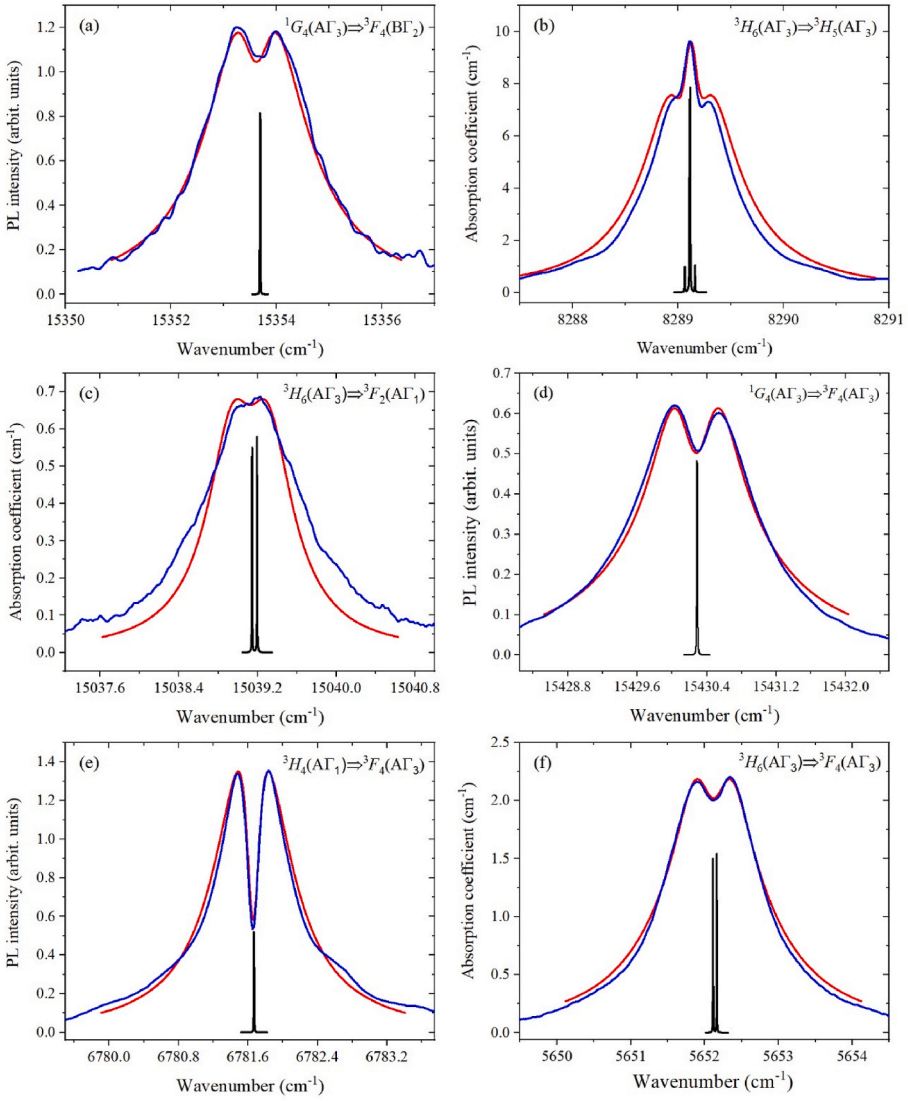

Fig. 4. (2 columns) Examples of the spectral line profiles in the high-resolution optical spectra of $LaAlO_3$:Tm^{3+}. Blue curves – experiment, red – simulations, black – calculated hyperfine structure (see Section 4). Assignment of the lines to the indicated transitions is explained in the text. (For interpretation of the references to colour in this figure legend, the reader is referred to the Web version of this article.)

The CF parameters B_p^k obtained from initial estimations in the framework of the exchange-charge model [30] and the subsequent fitting of the measured frequencies of optical transitions are presented and compared with the literature data [22,27,29,31] in Table 2. To fit the centers of gravity of optical multiplets, the free-ion parameters [28] were slightly corrected, in particular, we used $\zeta = 2629$, $F^2 = 102250$, $F^4 = 73300$, and $F^6 = 55600$ cm^{-1}.

Next, we have a possibility to estimate the concentration c_{Tm} of Tm^{3+} ions in the studied sample by making use of the measured magnetization. The quantum-statistical expression for a magnetic moment averaged over equally distributed four types of domains is written as follows

$$M(B) = \int_0^{\pi} \frac{\mathrm{Tr}[m_z \exp(-H_B/kT)]}{2\mathrm{Tr}[\exp(-H_B/kT)]} \cos\theta \sin\theta d\theta, \quad (4)$$

where $H_B = H_0 + m_z B \cos\theta$ is the Hamiltonian of a Tm^{3+} ion with the magnetic moment operator m_z along the symmetry axis of a domain in the magnetic field $\boldsymbol{B}$, k is the Boltzmann constant, and θ is the angle between the field $\boldsymbol{B}$ and a domain symmetry axis. The measured magnetization in the field $B = 9$ T at $T = 2$ K equals 0.204 emu/g, and, using the nominal concentration 0.5 wt%, we obtain the magnetic moment 1.19 μ_B per Tm^{3+} ion (μ_B is the Bohr magneton). From a comparison of this moment with the calculated one, $M(B) = 2.56$ μ_B, we obtain the real concentration $c_{Tm} = 0.232$ wt%. The corresponding calculated field dependence of the magnetization is compared with the experimental data in Fig. 5. The relatively small difference between the calculated and measured magnetization curves in weak magnetic fields (Fig. 5) points to a possibility of inhomogeneous distribution of ferroelastic domains over four trigonal symmetry axes of the parent cubic phase.

The single stable thulium isotope (^{169}Tm) has the non-zero nuclear spin moment $I = 1/2$ (nuclear gyromagnetic ratio $\gamma_n = -3.54$ MHz/T [32]). The obtained CF parameters are further used to calculate the hyperfine structure of the CF levels of impurity Tm^{3+} ions in $LaAlO_3$. The total single-ion Hamiltonian operating in the space of $91(2I+1)$ electron-nuclear states can be written as follows:

$$H = H_0 + H_{HFM}, \quad (5)$$

where H_{HFM} is the energy of the magnetic hyperfine interaction. The explicit expression for the operator H_{HFM} is presented in Ref. [33]. The energies of the electron-nuclear sublevels of CF energy levels were

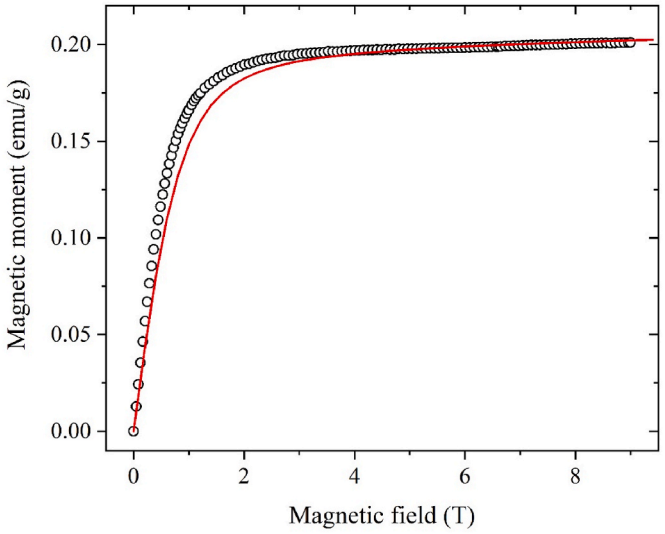

Fig. 5. Measured (symbols) and calculated (red solid line, see Section 4) magnetization of LAO:Tm^{3+} ($T = 2$ K). (For interpretation of the references to colour in this figure legend, the reader is referred to the Web version of this article.)

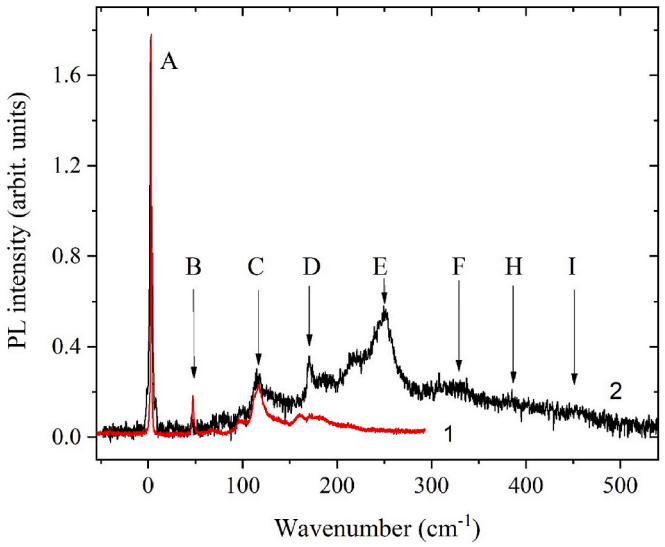

Fig. 6. PL spectra corresponding to transitions from the CF singlet $^3H_4(A\Gamma_1)$ (red line 1) and CF doublet $^3F_4(A\Gamma_3)$ (black line 2) to CF sublevels of the ground multiplet $^3H_6$ (the wavenumber axes in raw spectra are mirror reflected relative to the lines A at frequencies 12434 and 5652 cm $^{-1}$, respectively, and shifted to the common origin). The final states are labeled by capital letters according to Table 1. (For interpretation of the references to colour in this figure legend, the reader is referred to the Web version of this article.)

computed by numerical diagonalization of the Hamiltonian of Eq. (5).

In the first order of the perturbation theory, the magnetic hyperfine interaction does not change energies of electronic singlets Γ_1 and Γ_2, but splits the Γ_3 doublets into two doublet electron-nuclear sublevels in the spectrum of Tm^{3+}. The calculated g-factors and hyperfine splittings of non-Kramers doublets Γ_3 are presented in Table 1 (columns 6 and 7, respectively). Fig. 4*a–f* shows that the calculated hyperfine splittings of the CF doublets are significantly smaller than the measured intervals in fine structures of the spectral lines. This result clearly indicates the necessity to take into account the electron-deformation interaction.

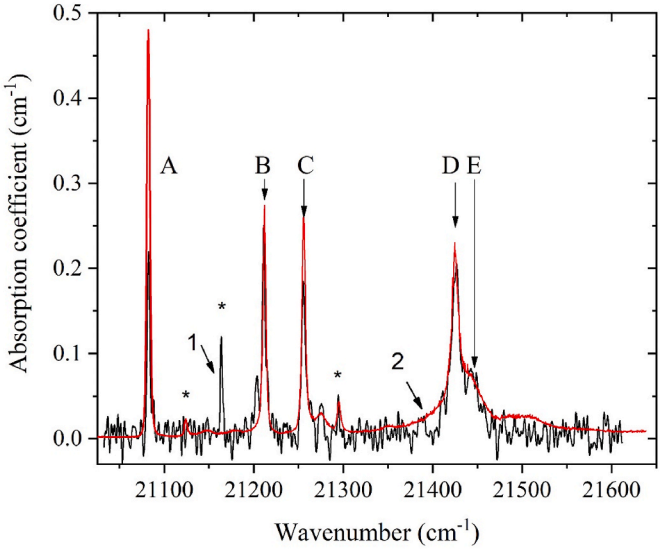

Fig. 7. Absorption (black line 1) and site-selective excitation (red line 2) spectra at frequencies of the $^1G_4$ optical multiplet. Stars mark the spectral lines of unknown nature. (For interpretation of the references to colour in this figure legend, the reader is referred to the Web version of this article.)

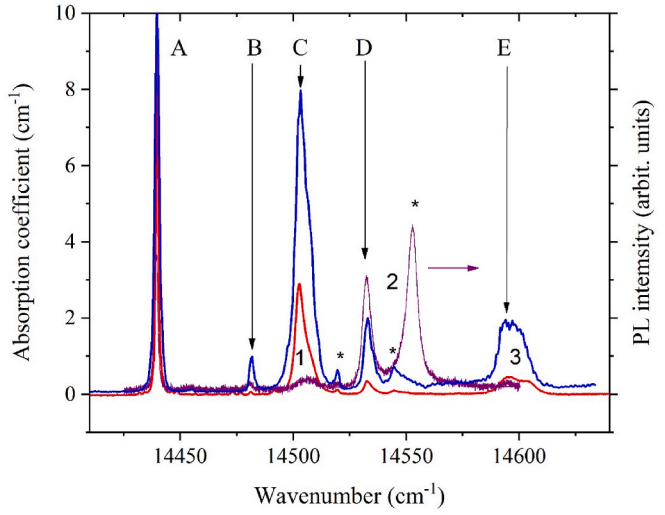

Fig. 8. Optical multiplet $^3F_3$ in the absorption $^3H_6(A\Gamma_3) \Rightarrow {}^3F_3$ (red line1), PL $^1G_4(A\Gamma_3) \Rightarrow {}^3F_3$ (violet line 2) and site-selective excitation (blue line 3) spectra. Spectral lines marked by stars are not identified. Capital letters denote CF levels of the $^3F_3$ multiplet with energies presented in Table 1, column 3. The wavenumber axis in the PL spectrum is transformed similarly to Fig. 6. (For interpretation of the references to colour in this figure legend, the reader is referred to the Web version of this article.)

5. Modeling of deformational fine structures of spectral lines

5.1. Electron-deformation interaction

In the linear approximation, the interaction of 4*f* electrons with the crystal lattice deformations is defined by the operator

$$H_{\text{el-def}} = \sum_{\Gamma,\lambda} V(\Gamma,\lambda) e(\Gamma,\lambda), \tag{6}$$

where $e(\Gamma,\lambda)$ are linear combinations of the deformation tensor components that transform according to the line λ of the IR Γ of the point symmetry group D_3:

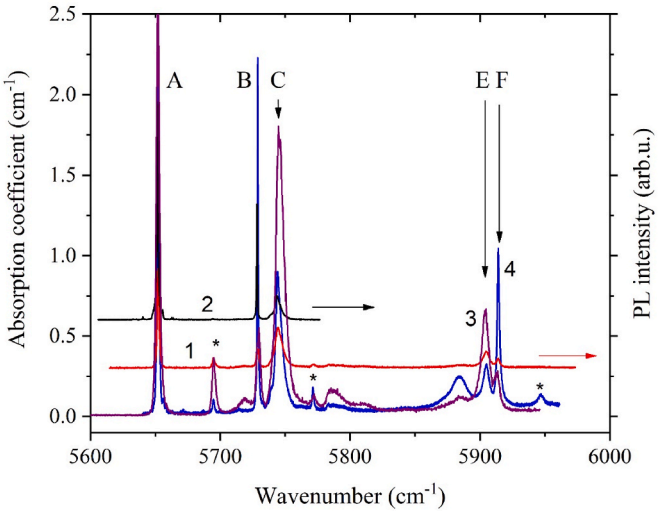

Fig. 9. Optical multiplet $^3F_4$ in the PL spectra [non-resonant excitations of the lowest sublevels of the $^1G_4$ (red line 1) and $^3H_4$ (black line 2) multiplets by the radiation with the 472 nm wavelength and the resonant excitation of the $^1G_4(D\Gamma_1)$ level (violet line 3)] and in the absorption spectrum (blue line 4). The wavenumber axes in PL spectra are transformed similarly to Fig. 6. Capital letters denote CF sublevels of the $^3F_4$ multiplet. (For interpretation of the references to colour in this figure legend, the reader is referred to the Web version of this article.)

Table 2
Crystal-field parameters B_p^k (cm^{-1}) for RE ions in $LaAlO_3$.

$p\ k$	Pr^{3+} [29]	Nd^{3+} [31]	Ho^{3+} [22]	Er^{3+} [27]	Tm^{3+}
2 0	−138.6	−229	−318	−318	−306
4 0	588	501	299	294	254
4 3	−604.5	−511	−279	−269	−255.5
6 0	−1836.8	−1670	−988	−988	−879.2
6 3	−951.3	−783	−595	−595	−626.0
6 6	−1177.2	−1352	−616	−616	−605.5

$$e(\Gamma_1^1) = (e_{xx} + e_{yy} + e_{zz}) \Big/ \sqrt{6},\ e(\Gamma_1^2) = (2e_{zz} - e_{xx} - e_{yy}) \Big/ \sqrt{12} \tag{7}$$

$$e(\Gamma_3^1, 1) = (e_{xx} - e_{yy}) / 2,\ e(\Gamma_3^1, 2) = e_{xy}, \tag{8}$$

$$e(\Gamma_3^2, 1) = e_{xz},\ e(\Gamma_3^2, 2) = -e_{yz}, \tag{9}$$

and the electronic operators are written as follows:

$$V(\Gamma, \lambda) = \sum_{pk} b_p^k(\Gamma, \lambda) O_p^k. \tag{10}$$

Here, operators O_p^k are linear combinations of spherical tensor operators $C_k^{(p)}$ and $C_{-k}^{(p)}$ which coincide with Stevens operators in the basis of eigenfunctions $|J, J_z>$ of the angular momentum [34]. Parameters of the electron-defoemation interaction $b_p^k(\Gamma, \lambda)$ used below in simulations of the deformational splittings and broadening of spectral lines were calculated in the framework of the exchange-charge model [30] in the system of coordinates defined above for Eq. (3). In the case of the interaction with degenerate deformations transforming according to the Γ_3 IR, the following relations are obtained from symmetry considerations:

$b_p^{-1}(\Gamma_3^n, 2) = -b_p^1(\Gamma_3^n, 1)$, for p = 2,4,6; $b_p^{-4}(\Gamma_3^n, 2) = -b_p^4(\Gamma_3^n, 1)$, for $p = 4,6$; $n = 1,2$;

$b_p^{-2}(\Gamma_3^n, 2) = b_p^2(\Gamma^n, 1)$, for $p = 2,4,6$; $b_6^{-5}(\Gamma_3^n, 2) = b_6^5(\Gamma_3^n, 1)$, $n = 1,2$.

Values of independent parameters are presented in Table 3.

Table 3
Calculated parameters of the electron-deformation interaction $b_p^k(\Gamma, \lambda)$ in units of 10^2 cm^{-1}.

$p\ k$	$b_p^k(\Gamma_1^2)$	$p\ k$	$b_p^k(\Gamma_3^1, 1)$	$p\ k$	$b_p^k(\Gamma_3^2, 1)$
2 0	−11.55	2 1	−25.19	2 1	2.66
4 0	3.80	2 2	−16.04	2 2	−12.60
4 3	−13.08	4 1	−11.06	4 1	−36.20
6 0	−0.02	4 2	8.31	4 2	−14.70
6 3	−10.94	4 4	31.98	4 4	0.51
6 6	−10.12	6 1	−1.37	6 1	3.63
		6 2	−4.24	6 2	−5.47
		6 4	−8.64	6 4	−0.57
		6 5	2.51	6 5	−18.43

5.2. Simulations of the shapes of spectral lines

Deformations of the crystal lattice of LAO (compression along one of the four C_3 axes) induce four possible twin-domain states [18,19]. There are three rhombohedral twin boundary arrangements in accordance with possible planes of contact: pure {100} or {110}, and mixed {100}/{110} [19,35]. In the pseudo-cubic coordinate frame with the C_4 axes, spontaneous deformations which transform the crystal from the cubic into the rhombohedral phase in four types of domains are determined by the following non-zero deformation tensor components [18]:

$$\mathrm{I}\left\{e_{xy}^{(cub)}, e_{xz}^{(cub)}, e_{yz}^{(cub)}\right\},\ \mathrm{II}\left\{e_{xy}^{(cub)}, e_{xz}^{(cub)}, -e_{yz}^{(cub)}\right\},\ \mathrm{III}\left\{e_{xy}^{(cub)}, e_{xz}^{(cub)}, -e_{yz}^{(cub)}\right\},\ \mathrm{IV}\left\{-e_{xy}^{(cub)}, -e_{xz}^{(cub)}, e_{yz}^{(cub)}\right\},$$

but all three shear deformations $e_{\alpha\beta}^{(cub)}$ ($\alpha \neq \beta$) have equal values. Let us consider a couple of domains, for example, of I and II types, contacting trough the {001} twin boundary, i.e., the *xy* face of the parent cubic cell. We assume that in this case the spontaneous shear deformation $e_{xy}^{(cub)}$ is fixed within the contacting domains volume, but the competition of shear deformations in the *xz* and *yz* planes having opposite signs and the conservation of the sample volume at the phase transition [19] bring about random shear deformations δe_{xz} and δe_{yz}. Using the transformation from the crystallographic frame of the parent cubic phase to the Cartesian frame defined above for Eq. (3), we obtain the Hamiltonian of the electron-deformation interaction in the following form (note, shear deformations do not induce the fully symmetric deformation $e(\Gamma_1^1)$ that corresponds to volume changes):

$$H_{el-def} = \left[\sqrt{3}V(\Gamma_1^2) - V(\Gamma_3^1, 1) + V(\Gamma_3^2, 1)\Big/\sqrt{2}\right](\delta e_{xz} + \delta e_{yz})\Big/3 + \left[-V(\Gamma_3^1, 2)\Big/\sqrt{2} + V(\Gamma_3^2, 2)\right](\delta e_{xz} - \delta e_{yz})\Big/\sqrt{3}. \tag{11}$$

The electronic operator $V(\Gamma_1^2)$ provides random shifts of CF energy levels and, in particular, just this term in the electron-deformation interaction is responsible for the deformational broadening of singlet-singlet transitions. Operators $V(\Gamma_3^n, \lambda)$ mix the wave functions of a non-Kramers Γ_3 doublet and are responsible for the corresponding deformational splitting.

Simulations of the profiles of the spectral lines with the resolved fine structure were performed by making use of the distribution function of shear deformations $u = \delta e_{xz}$ and $v = \delta e_{yz}$ represented by the two-dimensional generalized Lorentz distribution similar to a distribution function of random deformations induced by point defects and forming a basis of an irreducible degenerate (two-dimensional) representation of the factor-group of a crystal lattice [24,26]:

$$g(u, v) = \gamma\left[2\pi\left(u^2 + v^2 + \gamma^2\right)^{3/2}\right]^{-1}. \tag{12}$$

The envelope of the spectral line corresponding to the optical transition between CF levels Γ and Γ' with the energies E_{Γ} and $E_{\Gamma'}$ in the absorption (emission) spectrum is computed by averaging the sum of

form-functions of individual MD or ED transitions between the electron-nuclear sublevels of the CF levels in the field of fixed deformations u and v over the distribution function (12). The form-function is approximated by a Gaussian

$$I_{0,\Gamma\Gamma'}(x) = \left(2\pi\delta^2_{\Gamma\Gamma'}\right)^{-1/2} \exp\left(-x^2 / 2\delta^2_{\Gamma\Gamma'}\right) \quad (13)$$

with the fitting parameter $\delta_{\Gamma\Gamma'}$, and the intensity distribution in the spectral line is given by the following expression:

$$I_{\Gamma\Gamma'}(\omega) = \int g(u,v) \sum_{k,k'} w^{kk'}_{\Gamma\Gamma'}(u,v) I_{0,\Gamma\Gamma'}\left(\hbar\omega - \varepsilon^{kk'}_{\Gamma\Gamma'}(u,v)\right) du dv. \quad (14)$$

Here, $\varepsilon^{kk'}_{\Gamma\Gamma'} = E_{\Gamma' k'} - E_{\Gamma k}$, $E_{\Gamma k}$ are energies of the sublevels of the CF level split by the hyperfine and electron-deformation interactions, $w^{kk'}_{\Gamma\Gamma'}$ is the integral probability of the transition between electron-nuclear states Γk and $\Gamma' k'$ induced by the radiation field. In the case of a multidomain sample, $w^{kk'}_{\Gamma\Gamma'}$ is proportional to the sum of squared absolute values of matrix elements of all components of the electronic magnetic or electric dipole moment of the ion. At temperatures studied, we can neglect differences of populations of the sublevels of the electronic CF states. The intensity distributions (14) with a frequency step of 10^{-4} cm^{-1} were obtained using the numerical integration over the uv-plane in the cylindric system of coordinates ($u = \rho \cos\varphi$, $v = \rho \sin\varphi$). Computations involved numerical diagonalization of the total Hamiltonian $H_{\text{tot}} = H + H_{\text{el-def}}$ (having eigenvalues $E_{\Gamma k}$) for each pair of variables ρ and φ with steps of $\gamma/15$ and $\pi/80$, respectively. The corresponding eigenfunctions were used to calculate matrix elements of the magnetic dipole moment.

The intensity distributions (14) in spectral lines corresponding to ED and MD singlet-doublet transitions have the same shape where the width of a dip at the line center is close to the most probable deformational splitting of the CF doublet. A specific feature of the doublet-doublet transitions is the strong dependence of the corresponding spectral line profile on relative values of the deformational splittings of the doublets participating in the optical transition and of the integral probabilities for sixteen ED or MD transitions between the hyperfine sublevels of the CF doublets. In the simulations of doublet-doublet transitions, the ratio between integral probabilities of ED and MD transitions was considered as an additional fitting parameter. In particular, the simulated specific shape of the triplet fine structure of the spectral line $^3H_6(A\Gamma_3) \Rightarrow {}^3H_5(A\Gamma_3)$ (see Fig. 4b) follows not only from the approximately equal deformational splittings of both CF doublets but, as well, from the seven times larger probabilities of ED transitions contributing to the wings of the line as compared to the MD ones at the line center.

The simulated line profiles which reproduce satisfactorily the measured ones (see Fig. 4*a–f*) were computed using the fitting parameters, namely, widths $\delta_{\Gamma\Gamma'}$ of individual transitions between the hyperfine sublevels of the CF levels and widths γ of the distribution function of random deformations, 0.092 ± 0.048 cm^{-1} and $(7 \pm 0.5) \cdot 10^{-4}$, respectively. The width γ of the distribution function $g(u,v)$ is a characteristic of a sample, not of a spectral line, and the obtained relatively narrow range of γ values from independent fitting procedures of profiles of different spectral lines validates the approach derived in the present work.

6. Conclusions

The structural transition from the cubic to trigonal phase in $LaAlO_3$ perovskite at 813 K is accompanied by the formation of a multidomain microscopically inhomogeneous structure and the appearance of rather large random deformations of the crystal lattice induced by domain boundaries. In the present work, the deformation field is studied by means of high-resolution optical spectroscopy of a $LaAlO_3$ single crystal doped with Tm^{3+} ions (0.5 wt%).

The registered spectral lines corresponding to transitions between CF levels of the impurity Tm^{3+} ions at the La^{3+} sites with the D_3 point symmetry in the absorption, photoluminescence, site-selective emission and excitation spectra are identified and related to specific initial and final states of the Tm^{3+} ion. The doublet degeneracy of the ground state of the Tm^{3+} ion is found from the low-temperature magnetization measurements. Values of the CF parameters are determined and physically grounded by initial calculations in the framework of the exchange-charge model. The observed anomalously strong broadening of spectral lines and the doublet or triplet structure of spectral lines are explained as a result of the interaction of the Tm^{3+} ions with random lattice deformations induced by boundaries of domains with different directions of spontaneous deformations along four trigonal symmetry axes of the parent cubic phase. Simulations of the line profiles based on the two-dimensional distribution function of random strains with the width of $(7 \pm 0.5) \cdot 10^{-4}$ reproduced satisfactorily the experimental data.

CRediT authorship contribution statement

K.N.B.: Measurements, data analysis, preparation. N.M.A.: Theory, software, simulations. I.E.M.: Measurements. S.I.N.: Analysis. Methodology. B.Z.M.: Conceptualization. Theory. Writing – original draft, preparation. R.V.Yu.: Magnetometry. M.N.P.: Supervision. Writing – review & editing.

Declaration of competing interest

The authors declare that they have no known competing financial interests or personal relationships that could have appeared to influence the work reported in this paper.

Acknowledgments

N.M.A. is grateful for a support from the Russian Foundation for Basic Researches (Project №19-32-90044). K.N.B. acknowledges a financial support from the Russian Science Foundation (Grant №19-72-10132). M.N.P. thanks the Ministry of Science and Higher Education of Russia under Grant 0039-2019-0004. The authors are grateful to Prof. P. J. Deren for the sample studied in the present work.

References

[1] W.Y. Lee, J. Vazquez, T.C. Huang, R. Savoy, Tl-based high-Tc superconducting thin films on $LaAlO_3$ substrates, J. Appl. Phys. 70 (1991) 3952–3954, https://doi.org/10.1063/1.349208, 120-K.

[2] M.T. Yurtcan, Deposition of grid-like single-crystal Ce_2O_3 thin films on $LaAlO_3$(100) substrate by pulsed laser deposition, J. Mater. Sci. Mater. Electron. 32 (2021) 3854–3862, https://doi.org/10.1007/s10854-020-05129-1.

[3] P. Venkataswamy, M. Sudheera, K. Vaishnavi, K. Ramaswamy, G. Ravi, M. Vithal, A new Ag/AgBr/$LaAlO_3$ plasmonic composite: synthesis, characterization, and visible-light driven photocatalytic activity, J. Electron. Mater. 49 (2020) 2358–2370, https://doi.org/10.1007/s11664-019-07938-5.

[4] X.B. Lu, H.B. Lu, Z.H. Chen, X. Zhang, R. Huang, H.W. Zhou, X.P. Wang, B. Y. Nguyen, C.Z. Wang, W.F. Xiang, M. He, B.L. Cheng, Field-effect transistors with $LaAlO_3$ and $LaAlO_xN_y$ gate dielectrics deposited by laser molecular-beam epitaxy, Appl. Phys. Lett. 85 (2004) 3543–3545, https://doi.org/10.1063/1.1806547.

[5] M. Esro, R. Mazzocco, G. Vourlias, O. Kolosov, A. Kreir, W.I. Milne, Solution processed lanthanum aluminate gate dielectrics for use in metal oxide-based thin film transistors, Appl. Phys. Lett. 106 (2015), 203507, https://doi.org/10.1063/1.4921262.

[6] P.J. Deren, J.-C. Krupa, Spectroscopic investigations of $LaAlO_3$:Eu^{3+}, J. Lumin. 102–103 (2003) 386–390, https://doi.org/10.1016/S0022-2313(02)00529-X.

[7] V. Singh, S. Watanabe, T.K.G. Rao, J.F.D. Chubaci, H.-Y. Kwak, Characterization, photoluminescence, thermally stimulated luminescence and electron spin resonance studies of Eu^{3+} doped $LaAlO_3$ phosphor, Solid State Sci. 13 (2011) 66–71, https://doi.org/10.1016/j.solidstatesciences.2010.10.010.

[8] A.M. Hernández, M.A. de León Alfaro, A.B. Villatoro, C. Falcony, T.R. Montalvo, J. Z. Medina, Luminescence characteristics of $LaAlO_3$:Eu^{3+} obtained by modified Pechini's method, Open J. Synth. Theor. Appl. 6 (2017) 1–12, https://doi.org/10.4236/ojsta.2017.61001.

[9] P.J. Deren, J.-C. Krupa, Spectroscopic properties of $LaAlO_3$ crystal doped with Ho^{3+}, J. Alloys Compd. 380 (2004) 362–367, https://doi.org/10.1016/j.jallcom.2004.03.061.

[10] P.J. Deren, R. Mahiou, Spectroscopic characterization of $LaAlO_3$ crystal doped with Er^{3+} ions, Opt. Mater. 29 (2007) 766–772, https://doi.org/10.1016/j.optmat.2005.12.006.
[11] M. Mączka, E. Mendoza-Mendoza, A.F. Fuentes, K. Lemański, P. Deren, Low-temperature synthesis, luminescence, and phonon properties of Er and/or Dy doped $LaAlO_3$ nanopowders, J. Solid State Chem. 187 (2012) 249–257, https://doi.org/10.1016/j.jssc.2012.01.028.
[12] P.J. Deren, R. Mahiou, Ph Goldner, Multiphonon transitions in $LaAlO_3$ doped with rare earth ions, Opt. Mater. 31 (2009) 465–469, https://doi.org/10.1016/j.optmat.2007.10.016.
[13] J. Pejchal, J. Barta, T. Trojek, R. Kucerkova, A. Beitlerova, M. Nikl, Luminescence and scintillation properties of rare-earth-doped $LaAlO_3$ single crystals, Radiat. Meas. 121 (2019) 26–31, https://doi.org/10.1016/j.radmeas.2018.11.010.
[14] P.J. Deren, A. Bednarkiewicz, Ph Goldner, O. Guillot-Noël, Laser action in $LaAlO_3$: Nd^{3+} single crystal, J. Appl. Phys. 103 (2008), 043102, https://doi.org/10.1063/1.2842399.
[15] S.-G. Lim, S. Kriventsov, T.N. Jackson, J.H. Haeni, D.G. Schlom, A.M. Balbashov, R. Uecker, P. Reiche, J.L. Freeouf, G. Lucovsky, Dielectric functions and optical bandgaps of high- K dielectrics for metal-oxide semiconductor field-effect transistors by far ultraviolet spectroscopic ellipsometry, J. Appl. Phys. 91 (2002) 4500–4505, https://doi.org/10.1063/1.1456246.
[16] C. Howard, B.J. Kennedy, B.C. Chakoumakos, Neutron powder diffraction study of rhombohedral rare-earth aluminates and the rhombohedral to cubic phase transition, J. Phys. Condens. Matter 12 (2000) 349–365, https://doi.org/10.1088/0953-8984/12/4/301.
[17] S.A. Hayward, F.D. Morrison, S.A.T. Redfern, E.K.H. Salje, J.F. Scott, K.C. Knight, S. Tarantino, A.M. Glazer, V. Shuvaeva, P. Daniel, M. Zhang, M.A. Carpenter, Transformation processes in $LaAlO_3$: neutron diffraction, dielectric, thermal, optical, and Raman studies, Phys. Rev. B 72 (2005), 054110, https://doi.org/10.1103/PhysRevB.72.054110.
[18] S. Bueble, K. Knorr, E. Brecht, W.W. Schmahl, Influence of the ferroelastic twin domain structure on the {100} surface morphology of $LaAlO_3$/HTSC substrates, Surf. Sci. 400 (1998) 345–355, https://doi.org/10.1016/S0039-6028(97)00891-1.
[19] P.A. Vermeulen, A. Kumar, G.H. ten Brink, G.R. Blake, B.J. Kooi, Unravelling the domain structures in GeTe and $LaAlO_3$, Cryst. Growth Des. 16 (2016) 5915–5922, https://doi.org/10.1021/acs.cgd.6b00960.
[20] P.J. Deren, Spectroscopic characterization of $LaAlO_3$ crystal doped with Pr^{3+} ions, J. Lumiun. 122–123 (2007) 40–43, https://doi.org/10.1016/j.jlumin.2006.01.081.
[21] A. Gocalinska, P.J. Deren, P. Gluchowski, Ph Goldner, O. Guiollot-Noël, Spectroscopic characterization of $LaAlO_3$ crystal doped with Tm^{3+} ions, Opt. Mater. 30 (2008) 680–683, https://doi.org/10.1016/j.optmat.2007.02.007.
[22] K.N. Boldyrev, N.M. Abishev, I.E. Mumdzi, S.I. Nikitin, P.J. Deren, B.Z. Malkin, M. N. Popova, Disorder effects in $LaAlO_3$:Ho^{3+} single crystals revealed by optical spectra, Phys. Rev. B 103 (2021), 054105, https://doi.org/10.1103/PhysRevB.103.054103.
[23] S.A. Klimin, D.S. Pytalev, M.N. Popova, B.Z. Malkin, M.V. Vanyunin, S. L. Korableva, High-resolution optical spectroscopy of Tm^{3+} ions in $LiYF_4$: crystal-field energies, hyperfine and deformation splittings, and the isotopic structure, Phys. Rev. B 81 (2010), 045113, https://doi.org/10.1103/PhysRevB.81.045113.
[24] N.M. Abishev, E.I. Baibekov, B.Z. Malkin, M.N. Popova, D.S. Pytalev, S.A. Klimin, Deformation broadening and the fine structure of spectral lines in optical spectra of dielectric crystals containing rare-earth ions, Phys. Solid State 61 (2019) 795–801, https://doi.org/10.1134/S1063783419050020 [Fiz. Tverdogo Tela 61 (2019) 898-904, 10.21883/FTT.2019.05.47589.22F.
[25] B.Z. Malkin, D.S. Pytalev, M.N. Popova, E.I. Baibekov, M.L. Falin, K.I. Gerasimov, N.M. Khaidukov, Random lattice deformations in rare earth doped cubic hexafluoroelpasolites: high-resolution optical spectroscopy and theoretical studies, Phys. Rev. B 86 (2012), 134110, https://doi.org/10.1103/PhysRevB.86.115124.
[26] B.Z. Malkin, N.M. Abishev, E.I. Baibekov, D.S. Pytalev, K.N. Boldyrev, M. N. Popova, M. Bettinelli, Distribution function of random strains in elastically anisotropic continuum and defect strengths of impurity Tm^{3+} ions in crystals with the zircon structure, Phys. Rev. B 96 (2017), 014116, https://doi.org/10.1103/PhysRevB.96.014116.
[27] E. Antic-Fidancev, P.J. Deren, J.-C. Krupa, Energy levels and crystal field calculations of Er^{3+} in $LaAlO_3$, J. Alloys Compd. 380 (2004) 376–379, https://doi.org/10.1016/j.jallcom.2004.03.063.
[28] W.T. Carnall, G.L. Goodman, K. Rajnak, R.S. Rana, A systematic analysis of the spectra of the lanthanides doped into single crystal LaF_3, J. Chem. Phys. 90 (1989) 3443–3457, https://doi.org/10.1063/1.455853.
[29] N. Pelletier-Allard, F. Martin-Brunetière, Étude théorique des spectres optiques des ions Pr^{3+} dans $AlLaO_3$, J. Phys. (Paris) 30 (1969) 849–855, https://doi.org/10.1051/jphys:019690030010083900.
[30] B.Z. Malkin, Crystal field and electron-phonon interaction in rare-earth ionic paramagnet, in: A.A. Kaplyanskii, R.M. Macfarlane (Eds.), Spectroscopy of Solids Containing Rare-Earth Ions, Elsevier Science Publishers, Amsterdam, 1987, pp. 13–49, https://doi.org/10.1016/B978-0-444-87051-3.50008-0. Ch. 2.
[31] M. Karbowiak, P. Gnutek, C. Rudowicz, Crystal-field analysis for RE^{3+} ions in laser materials: III. Energy levels for Nd^{3+} and Er^{3+} ions in $LaAlO_3$, $YAlO_3$, and $LaGaO_3$ single crystals – combined approach to low symmetry crystal field parameters, Chem. Phys. 400 (2012) 29–38, https://doi.org/10.1016/j.chemphys.2012.01.021.
[32] G.H. Fuller, Nuclear spins and moments, J. Phys. Chem. Ref. Data 5 (1976) 835–1092, https://doi.org/10.1063/1.555544.
[33] D.S. Pytalev, E.P. Chukalina, M.N. Popova, G.S. Shakurov, B.Z. Malkin, S. L. Korableva, Hyperfine interactions of Ho^{3+} ions in KY_3F_{10}: electron paramagnetic resonance and optical spectroscopy studies, Phys. Rev. B 86 (2012), 115124, https://doi.org/10.1103/PhysRevB.86.115124.
[34] V.V. Klekovkina, A.R. Zakirov, B.Z. Malkin, L.A. Kasatkina, Simulations of magnetic and magnetoelastic properties of $Tb_2Ti_2O_7$ in paramagnetic phase, J. Phys.: Conf. Ser. 324 (2011), 012036, https://doi.org/10.1088/1742-6596/324/1/012036.
[35] H. Fay, C.D. Brandle, Reorientation and detwinning of $LaAlO_3$ single crystals by mechanical stresses, J. Appl. Phys. 38 (1967) 3405–3408. https://doi.org/10.1068/1.1710126.